Exchange bias and size effects in Ni nanoparticles embedded in a mesoporous carbon matrix

Natalia M. Rinaldi – Montes[*]

[*] Departamento de Física, Universidad de Oviedo, c/ Calvo Sotelo s/n 33007, Oviedo, Spain

ABSTRACT

The exchange bias effect has been studied in a series of carbon coated NiO (shell) / Ni (core) nanoparticles with diameters ranging from 3 to50 nm. Using an easy single-step reaction particles were embedded inside the pores of a mesoporous activated carbon matrix. A joint-analysis has been made in order to assess the effects of the coupling between the ferromagnetic Ni cores and the antiferromagnetic NiO shells. The structural characterization of the samples has been studied by x-ray diffraction, transmission electron microscopy, and x-ray absorption spectroscopy. In addition, magnetic properties have been extensively investigated by measuring hysteresis loops and magnetization measurements in the 2-300 K temperature range, in zero-field-cooling and field-cooling conditions. It has been found that Ni/NiO nanoparticles present a moderate exchange bias (~ 400 Oe) due to the exchange coupling at the interface between Ni and NiO layers. Finally, the temperature and field dependences of this effect have been discussed taking into account the anisotropy and magnetism of the NiO component.

1. INTRODUCTION

Magnetic nanoparticles (MNPs) have been studied extensively due to their potential technological applications and special magnetic properties that differ considerably from those of their bulk counterparts[1-3]. From the fundamental point of view, magnetic NPs serve as canonical systems for investigating the Stoner–Wohlfarth and the Neèl–Brown models, to study finite-size effects or magnetic proximity effects. Most of the core–shell systems for potential applications have been prepared from oxidation of transition metal NPs, leading to interface exchange interactions between the core (typically ferromagnetic, FM) and the shell (antiferromagnetic, AFM or ferrimagnetic FIM). This core–shell morphology often gives rise to striking and independent mechanisms like the hysteresis-loop shift (the so called Exchange bias, EB, effect) and the coercivity (Hc) enhancement. On the other side, both high magnetization and coercivity are desirable for applications of nanoscale systems in high density, magnetic storage, hard magnets or magneto-electric devices. Among all transition metal NPs, nickel NPs exhibit unique magnetic and catalytic properties that make them

promising candidates for chemical separation procedures like heterogeneous catalysis, immobilization of biomolecules and adsorption of contaminants[4-12]. This possibility is due to the fact that superparamagnetic nickel NPs do not magnetically aggregate in solution without an applied magnetic field.

Magnetic porous materials are very important and useful in several branches of the high-tech chemical industry, like magnetic carriers for biomedicine (transport of anticancer drugs, heat treatment of tumors), magnetic resonance imaging and magnetic separation[13-15]. Most of the previous research has focused on polymer or silica based materials[16,17], but carbon-based magnetic porous materials are recently receiving more attention due to their biocompatibility and chemical stability and inertness[18-20]. Among this latter materials, activated carbon (AC) is one of the most interesting due to its extremely high degree of microporosity and thus its large surface area available for adsorption or chemical reactions. Partially filling the carbon matrix with magnetic NPs would allow the separation of the AC + reagent ensemble from the surrounding media just by applying a small gradient field.

In order to use innovative magnetic NPs for artificial engineering, a systematic characterization is needed to control not only the magnetic properties of an individual particle, but also the collective behavior of an ensemble of interacting magnetic NPs. In this study, we use a single-step reaction to prepare nickel NPs embedded inside the pores of a mesoporous activated carbon matrix. The average size of the NPs can be controlled by the temperature of the reaction. The purpose of this study is to find a correlation between size, microstructure, morphology and magnetic properties of the NPs. X-ray diffraction, transmission electron microscopy, and x-ray absorption spectroscopy were used to characterize the crystal structure and the morphology of the NPs. In addition, hysteresis loops and magnetization measurements in the 2-300 K temperature range, in zero-field-cooling and field-cooling conditions were performed in order to characterize their magnetic behavior. The interplay between the microstructure and magnetic response was also discussed.

2. MOTIVATION

Our group has developed an exhaustive study focused on the influence of the microstructure and morphology in the magnetic response of Fe, Co and Ni NPs embedded in an activated porous carbon[21-23]. The main results are: (i) a peculiar “onion-like” morphology in the case of Fe NPs with a γ -Fe core surrounded by concentric shells of ferromagnetic α-Fe and ferromagnetic maghemite, which allows the study of the γ-Fe magnetism, a subject of large controversy for more than 50 years[21], (ii) the existence of a moderate EB effect (H_{EB} ~ 1 kOe) in Co NPs with a metallic Co core / Co-oxide shell morphology, which is almost independent of the cooling applied magnetic field up to 85 kOe[22]. The latter finding has not been observed previously in other magnetic NP systems and could be of great interest for the understanding of the exchange bias effect in nanostructured materials. In both cases, Fe and Co NPs present the same magnetic saturation as their bulk counterparts, at room temperature. And (iii) the possibility of obtaining Ni-oxide free graphite-encapsulated Ni NPs with almost ideal superparamagnetic behaviour at room temperature by adding sucrose in the synthesis process[23]; these NPs exhibited a considerably

higher magnetization than their oxidized counterparts. On the other hand, spherical nickel NPs in the superparamagnetic state have been reported to have greatly decreased magnetic saturation at room temperature compared with bulk nickel[6,24-27]. Higher magnetization can be achieved for larger particle sizes, but this also increases the blocking temperature to near room temperature, with the particles becoming ferromagnetic and thus aggregated[25]. This change of magnetic properties is reported to be due to the particles being partially amorphous[25], the oxidation of the nickel[24] and the existence of a magnetic dead layer[28], which means the surface layer of a NP made of a ferromagnetic material, where the magnetic coupling can be highly frustrated, leading to a depletion of ferromagnetism and the appearance of misaligned spins. Also a great enhancement of the magnetic response at low temperature has been observed in nickel NPs[27]. Both effects become progressively more important as the size of the particle is reduced. Other studies point out the important role that the surrounding matrix play in the reduction of the magnetic volume of the NP with respect to its physical volume (determined by TEM measurements), finding an interdiffusion between matrix and NP atoms in Si and amorphous C matrices, while the structure of clusters embedded in metallic matrices (Ag, Au) remain intact[29].

Here, we present a comparative between the magnetic properties of a series of different sized nickel NPs, in order to check which of the factors mentioned above (amorphous structure, oxidation of nickel, magnetic dead layer or interdiffusion in the surrounding matrix) are responsible of the reduced magnetic saturation and the enhanced magnetic signal at low temperature reported for nickel NPs.

3. EXPERIMENTAL PROCEDURE

3.1. Chemical synthesis of the samples

A commercial activated carbon (AC) was employed as carbonaceous matrix for the deposition of nickel nanoparticles. The AC material which was supplied by Osaka Gas (Japan) has a large Brunauer-Emmett-Teller (BET) surface area of 2350 $m^2 \cdot g^{-1}$, a high pore volume of 1.47 $cm^3 \cdot g^{-1}$ and a porosity made up of mesopores of up 6-7 nm diameter and centered at around 2.5 nm. The synthetic method is based on pyrolysis taking place within the restricted volume formed by the AC porosity. As in a typical fabrication, 1 g of AC was impregnated up to incipient wetness with a solution formed by nickel nitrate (0.7 g) in 1 mL of water. The impregnated sample was dried and subsequently heat-treated under N_2 up to a chosen temperature (T_H) and kept at this temperature for 3 hours. Under these conditions, the decomposition of Ni salt into NiO takes place first. Subsequently, as the temperature rises, the NiO is reduced by means of carbon and nickel NPs are formed and rapidly oxidized into NiO at room temperature by the action of atmospheric oxygen. This process results in the formation of core@shell NPs made up of a Ni core, surrounded by a uniform-size NiO shell (Ni@NiO). Finally, the sample was cooled under nitrogen down to room temperature and then passivated with a small stream of air to stabilize it. As it will be shown in the subsequent paragraphs, the heating temperature (T_H) determines the average size of the NPs so that bigger NPs are obtained as T_H increases. Three different samples were synthesized at 673, 873 and 1023 K and named as A, B and C, respectively. The nickel content of these

samples was determined to be approximately 11% by thermogravimetric analysis (TGA).

3.2. Experimental details

TEM and HRTEM images were recorded on JEOL2000-EXII & JEOL-JEM-2100F microscopes (200 kV), respectively, on samples prepared by depositing a small amount of powder in ethanol and then by depositing several drops of this solution on carbon films which were placed on copper grids. Room temperature X-ray powder diffraction patterns were obtained using a Seifert 3000T/T diffractometer operating at 40 kV and 20 mA, using Cu *K*α radiation (λ=1.5406 Å). The room temperature Ni *K*-edge XANES spectra were recorded in transmission mode, at the BL01B1 beamline at Spring-8 (Japan). Ni metal foil spectra were also recorded simultaneously in order to calibrate the energy. For the measurements, homogeneous layers of the powdered samples were prepared by spreading the powder over an adhesive tape. The thickness and homogeneity of the samples were optimized to obtain the best signal-to-noise ratio. The absorption spectra were analyzed according to standard procedures and the spectra were normalized to the absorption coefficient averaged at high energy in order to eliminate the dependence of absorption on the sample thickness.

The temperature and magnetic field dependences of magnetization, *M(T,H)* were measured using a Quantum Design PPMS-14T magnetometer with the vibrating-sample (VSM) option. First, the sample was cooled in a zero field (ZFC) from 300 K down to 10 K. Then a magnetic field (H_a) was applied and kept constant. Afterward M_{ZFC} magnetization was measured by increasing the temperature from 10 K to 300 K at a sweeping rate of 1 K/min. Finally, M_{FC} was recorded while cooling the sample starting from 300 K until 10 K, also at a sweeping rate of 1 K/min. The magnetization *M(H)* was measured at a sweeping rate of 100 Oe/s between 0 and 14 T at room (300 K) and low temperature (2 K).

For measuring the exchange bias effect (EB), a field (H_{cool}) was applied to the sample at 150 K and kept constant meanwhile it was cooled down to 5 K; then a hysteresis loop was recorded between -5 T and 5 T, at a sweeping rate of 5 K/min. Afterward the sample was heated again until 150 K in order to repeat the process at several cooling fields. The EB field (H_{EB}) was defined as the shift of the central point of the hysteresis loop measured at a given H_{cool}, relative to the H_{cool} = 0 loop.

4. RESULTS AND DISCUSSION

4.1. Structural characterization

4.1.1. Transmission electron microscope

The carbonaceous matrix is formed by micrometric grains, each one of them has a sponge-like morphology with the NPs filling the interconnections between pores (see Figure 1a). As it was said before, samples A, B and C were prepared at increasing temperatures. The Ostwald ripening phenomenon[30] describes how small crystals or sol particles dissolve and redeposit onto larger ones. This nucleation process is thermodynamically driven by the balance between the surface and volume energies of the particles. So then, larger NPs nucleate at higher temperatures, being A the smallest and C the biggest one. In order to determine the distribution size of the samples, around 10000 NPs were counted, using the PSA macro for ImageJ[31], and modeled with

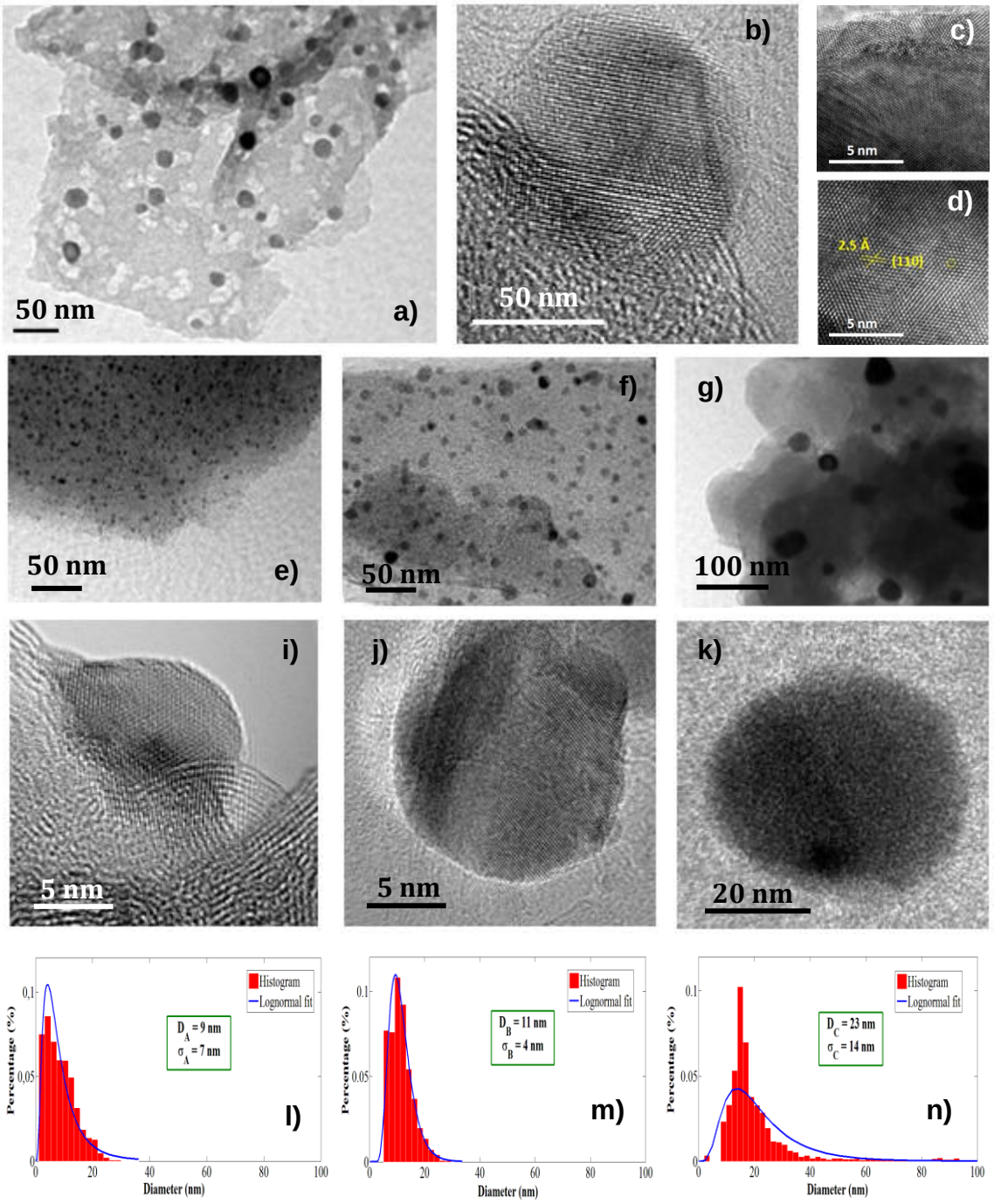

Figure 1. (a) TEM image of the sponge-like structure of the AC matrix, with NPs filling the interconnected pores. HRTEM image of a NP (b) whose central (d) and edge (c) regions have been expanded. The central region exhibits a face centered cubic structure in the (110) direction with an interatomic distance (d) of 2.5Å. The edge region shows a reduction of the interplanar distance, corresponding to NiO face centered cubic structure (d~2.1Å). TEM images of the A (e), B (f) and C (g) samples. HRTEM images of the A (i), B (j) and C (k) samples. Histograms (red bars) of the NP diameter together with fits (blue lines) to log-normal functions of A (l), B (m) and C (n) samples respectively. The mean particle sizes obtained are $D_A(\sigma_A)$ = 9(7) nm, $D_B(\sigma_B)$ = 11(4) nm and $D_C(\sigma_C)$ = 23(14) nm, respectively.

a lognormal fit. The average values (D) and standard deviations (σ) of the fitting distributions were found to be $D_A(\sigma_A)$ = 9(7) nm for sample A (see figure 1e,i,l), $D_B(\sigma_B)$ = 11(4) nm for sample B (see figure 1f, j, m) and $D_C(\sigma_C)$ = 23(14) nm for sample C (see figure 1g, k, n). These distributions are quite broad because nucleation does not take place uniformly throughout the whole volume so that NPs ranging from 3 to 50 nm were detected in every sample. This heterogeneity was manifested in the magnetic collective behavior of the system (see section 4.2). In figures 1c and 1d the edge and central regions, respectively, of the NP from figure 1b are showed; NPs exhibit an ordered face centered cubic (FCC) structure in the nucleus with an interatomic distance of d~2.5Å, corresponding to a Ni lattice along the (110) crystallographic direction. Approaching the edge, the interplanar distance decreases to d~2.2Å, very near to the first neighbor distance of NiO (2.1Å), which also crystallizes in FCC structure. This reduction is quite significant because in a single structure particle an increase of the interatomic distance is expected due to surface relaxation and lack of coordination. In order to strengthen this assumption, local EDX measurements were performed on several NPs, giving 100% of Ni for the central region composition and 70% Ni / 30% NiO for the edge zone.

4.1.2. X – ray diffraction

The XRD patterns (see figure 2) of the A (green), B (2 purple) and C (yellow) samples were fitted using the FullProf package, based on the Rietveld method[32]. It should be pointed out that the 90% of the samples is formed by carbon, so that it constitutes an important

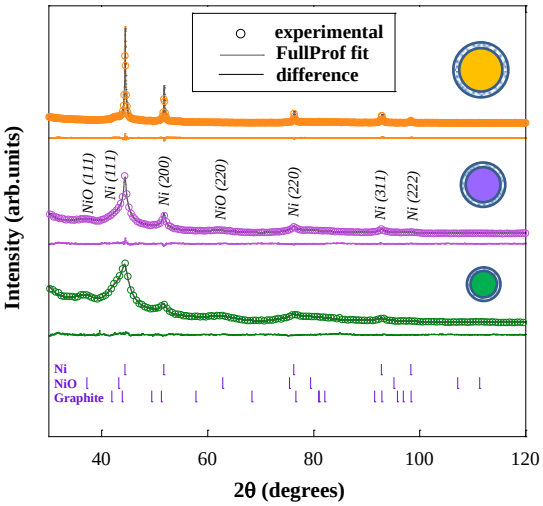

Figure 2. X-ray diffraction patterns of the A (green), B (purple) and C (yellow) samples. The Ni-FCC crystal structure is characterized by the positions of the (111), (200), (220), (311) and (222) Bragg peaks. The existence of a NiO- FCC phase can be deduced from the diffracted peaks associated to the (111) and (220) crystallographic directions. Only 30% of the points are showed for a better visualization.

background that introduces a certain ambiguity in the quantitative analysis of the patterns. Apart from this, it can be deduced that Ni crystalline NPs have a FCC crystal structure, in agreement with HRTEM measurements, and a cell parameter $a_{Ni\text{-}FCC}$ = 3.52(1) Å, which coincides with that of bulk FCC-nickel (3.52 Å). Also a NiO phase with FCC structure was included in order to fit the diffraction patterns properly; its cell parameter $a_{NiO\text{-}FCC}$ = 4.17(1) Å is very close to that of bulk FCC-NiO (4.18 Å). The average sizes of the NPs estimated from XRD measurements were 6(1) nm, 11(2) nm and 38(8) nm, for samples A, B and C, respectively. This is consistent with the fact that peaks get sharper as the size of the NPs increases. Nevertheless, that is a qualitative estimation, because XRD technique requires higher coherence lengths in order to provide quantitative information.

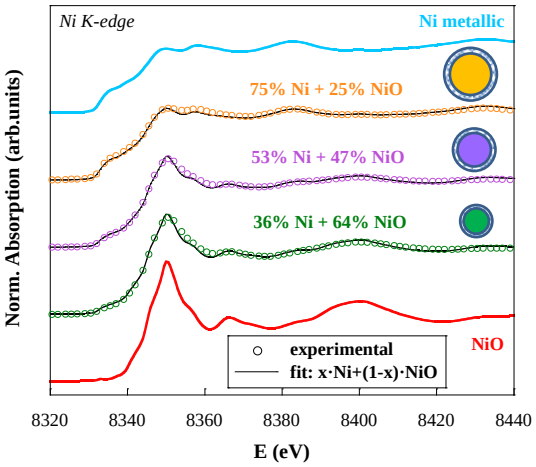

Figure 3. Ni *K*-edge XANES spectra for the A (green), B (purple) and C (yellow) samples and for the Ni and NiO standards, measured at room temperature. The experimental data are represented with open circles and the simu lation with solid lines. Only 30% of the points are showed for a better visualization. The optimum weighted combination of Ni and NiO spectra that fit the pattern of each sample was calculated by least square method and the results are displayed above the corresponding spectrum.

4.1.3. X – ray absorption spectroscopy

Ni K-edge XANES spectra of A, B and C samples and of NiO and Ni standards were recorded at room temperature (see figure 3). The XANES region of the absorption spectrum extends ~100 Å up from the edge and provides information about the local environment around the absorbing Ni atoms. The absorption process occurs when a photon is captured by a core electron and then a photo-electron is created and ejected. It can be scattered by the electrons of the neighboring atoms so that it may return to the initial absorbing atom. The absorption coefficient is strongly influenced by the existence of available states and therefore it is modified by the return of the photo-electron to the initial atom, giving rise to the observed spectrum. That is why partial contributions to the scattering of each neighboring atom can be added in order to simulate the resulting recorded XANES spectra. By XRD measurements just two species containing Ni were detected in the samples, so that each Ni absorbing atom just can be surrounded by an oxygen atom or by another Ni atom. Therefore, a weighted mixture of Ni and NiO spectra were used to fit the experimental XANES patterns, and the optimal combinations were calculated by least square method. The percentage of Ni atoms in each sample was found to be 36% for sample A, 53% for sample B and 75% for sample C. This result is in good agreement with previous measurements since HRTEM images showed that oxidized Ni atoms were located at the surface of the NPs and XRD fits pointed out that NPs from sample A were the smallest ones, on average, and those from sample C were the biggest ones. Therefore, the amount of surface (oxidized) atoms is more relevant in percentage as the size of the NPs decrease.

4.2. Magnetic characterization

4.2.1. Dependence of the magnetization with the field

The *M(H)* curves were recorded both at 300 K (see figure 4a) and at 2 K (see figure 4b) for samples A (green), B (purple) and C (yellow). The room temperature magnetization of every sample was fully saturated for field values higher than 5 kOe. The saturation magnetizations (M_S) were substantially lower than that of bulk nickel (55 emu/g), even though they increase with the average size of the NPs, given that M_S^A = 6 emu/g-Ni, M_S^B = 14 emu/g-Ni and M_S^C = 35 emu/g-Ni. As far as low temperature measurements are concerned, magnetization is saturated just for the biggest NPs, meanwhile the high field slope is more pronounced for smaller NPs. In every case, the maximum reached values are below the bulk Ni M_S, M_{max}^A = 28 emu/g-Ni, M_{max}^B = 25 emu/g-Ni

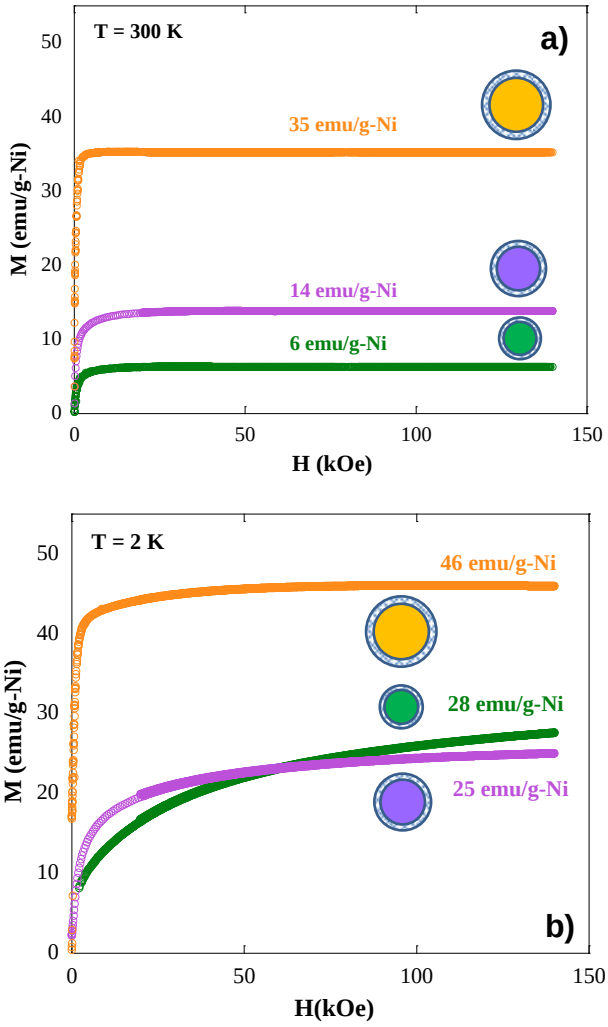

Figure 4. M(H) curves, normalized to the amount of Ni in the composite, for samples A (bottom), B (middle) and C (top), at room temperature, 300 K (a) and low temperature, 2 K (b). The maximum magnetization value is displayed near each curve. It should be noted that saturation (M_S) is reached at 5 kOe for room temperature measurements, meanwhile low temperature curves show a slope which is more pronounced in smaller NPs. It is worth noting that in all cases M_S is smaller than the bulk value (55 emu/g).

and M_{max}^{C} = 46 emu/g-Ni. It can be deduced that the reduction of M_S with respect to that of bulk nickel is due to the oxidation of surface atoms, forming NiO, which has an antiferromagnetic behavior and shows an almost negligible magnetic response to the application of an external field. Nevertheless, the assumption the just Ni atoms in pure Ni phase contribute to room temperature magnetization would predict the following percentages of Ni atoms for the studied samples: 11% for sample A, 25% for sample B and 64% for sample C; which considerably overestimate the amount of NiO in the samples, compared to XANES results. So another complementary possibility which can be deduced from the fact that the slope s of the non-saturated low temperature magnetizations were higher for smaller NPs is that surface atoms experience a reduced exchange field and thus it gives rise to a lack of ferromagnetic order, becoming random and paramagnetic[27]. Moreover, spin canting effect[33,34] occurs when ferromagnetic spins are nor perfectly aligned in a parallel orientation, but are canted by a few grades, resulting in a weaker moment. It also has been reported that the presence of interstitial oxygen atoms in the unit cell of Ni causes anomalous magnetic behaviors such as very large enhancement at low temperatures[35]. Finally, nickel atoms located at the interfaces between the NPs and the matrix can diffuse into the carbon giving rise to a paramagnetic and non-stoichiometric carbide[36].

4.2.2. Zero field cooling – field cooling

In figure 5a, M(T) curves measured in ZFC (red) –FC (blue) regimes, under different applied magnetic fields (H_{app}) ranging from 10 Oe to 1 kOe. Assuming that each NP constitute a monodomain with uniaxial symmetry, at very low temperature, $M_{ZFC}=M_{nr}^2 H_{eff} / 3K$, when all the NPs are blocked , where M_{nr} represents the nonrelaxing magnetization, K the anisotropy constant and H_{eff} the field seen by the particle; this means a balance between (H_{app}) and the

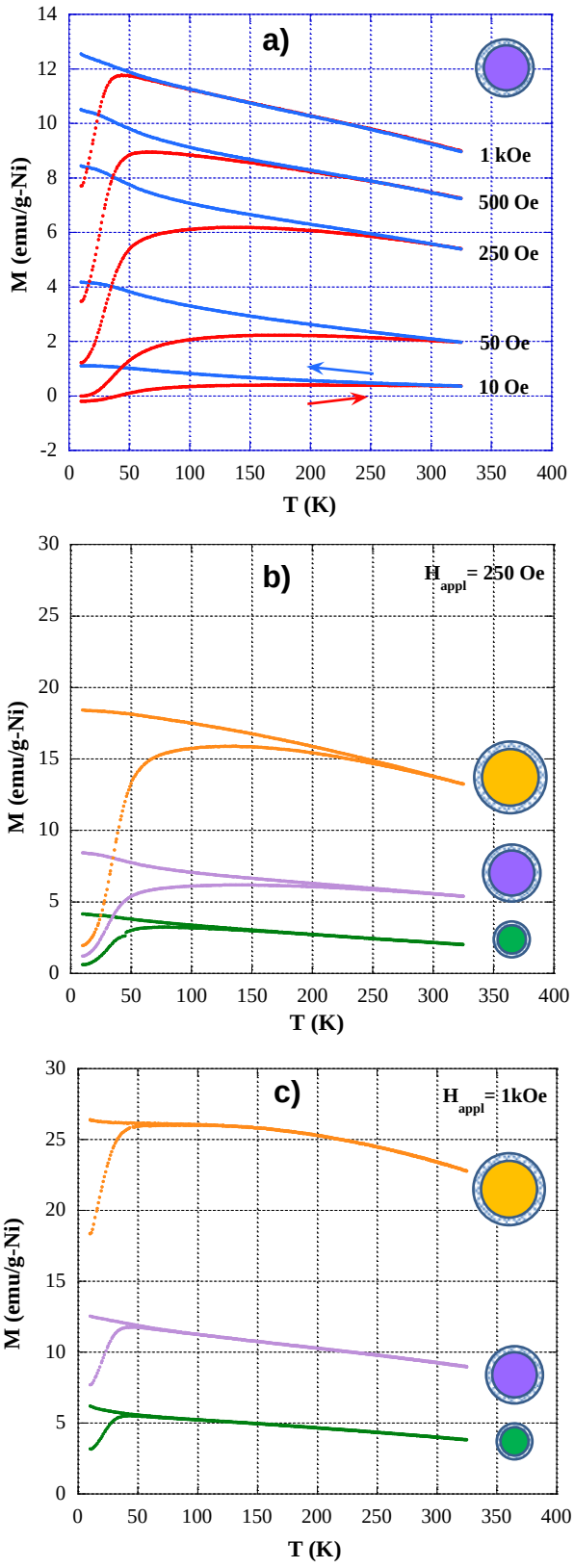

Figure 5. (a) M(T) curve in the ZFC (red line) – FC (blue line) regimes measured for sample B under applied magnetic fields (H_{app}) of 10 Oe, 50 Oe, 250 Oe, 500 Oe and 1 kOe. (b), (c) Dependence of the ZFC – FC curves with the average size of the samples A (green), B (purple) and C (yellow), for fixed applied fields of 250 Oe and 1 kOe.

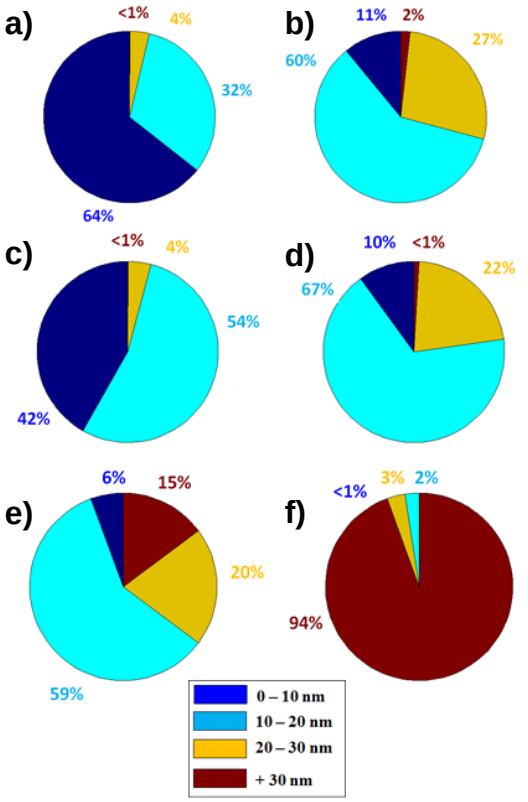

Figure 6. Pie charts showing the comparison between the number of NPs of a given size and the percentage relative to the total amount of magnetic moments that they constitute. It should be pointed out that distributions of figure 1 l, m, n just account for the number of NPs of a given size, but the magnetic response of the sample is determined by the amount of mass that behaves in a superparamagnetic, blocked or ferromagnetic way. Even if small NPs predominate in the sample their magnetic contribution can be negligible compared to that due to bigger NPs.

anisotropy energy[37]. As increasing the temperature, M_{ZFC} increases and shows a maximum at a certain temperature (T_B); afterward, M_{ZFC} decreases. On the other hand, M_{FC} overlaps with M_{ZFC} until the temperature of irreversibility (T_{irr}) and then continues to increase until it saturates and remains constant. It has been shown[37] that in systems with a well-defined size and no interactions between NPs, T_B and T_{irr} coincide. Instead, the broad size

distribution of this NPs (see figures 1 l, m and n) results in a ZFC-FC magnetization where the relaxation processes of all these NPs do not take place at the same temperature, so that the measured curves contain a superposition of all those phenomena. This gives rise to a broad maximum in the ZFC-FC which means that there is not a unique blocking temperature but a distribution. It is well known that T_B increases with the magnetic volume of the NPs (Néel equation[38]), so that the maximum of the ZFC curve corresponds to the T_B associated with the majority NPs. Following the same reasoning, in these systems the T_{irr} corresponds to the T_B of the biggest NPs present in the samples. So that sample C shows both the highest T_B and T_{irr}, as expected (see figure 5 b, c). Finally, smaller NPs (sample A) exhibit a ~1/T superparamagnetic behavior, meanwhile bigger NPs present a concave curvature of the ZFC-FC magnetization at temperatures lower than 350 K. It should be pointed out that distributions just account for the number of NPs of a given size, but the magnetic response of the sample is determined by the amount of magnetic moments that behaves in a superparamagnetic, blocked or ferromagnetic way. In figure 1, two pie charts are plotted for each sample; it can be deduced that, even if small NPs predominate in the sample their magnetic contribution can be negligible compared to that due to bigger NPs. Note that the monodomain size[39] for NPs is ~ 60nm.

4.2.3. Exchange bias

The EB is a phenomenon associated with the exchange anisotropy created at the interface between an AFM and a FM material[40,41], in this case, between the NiO shell and the Ni core. It can be observed when applying a static

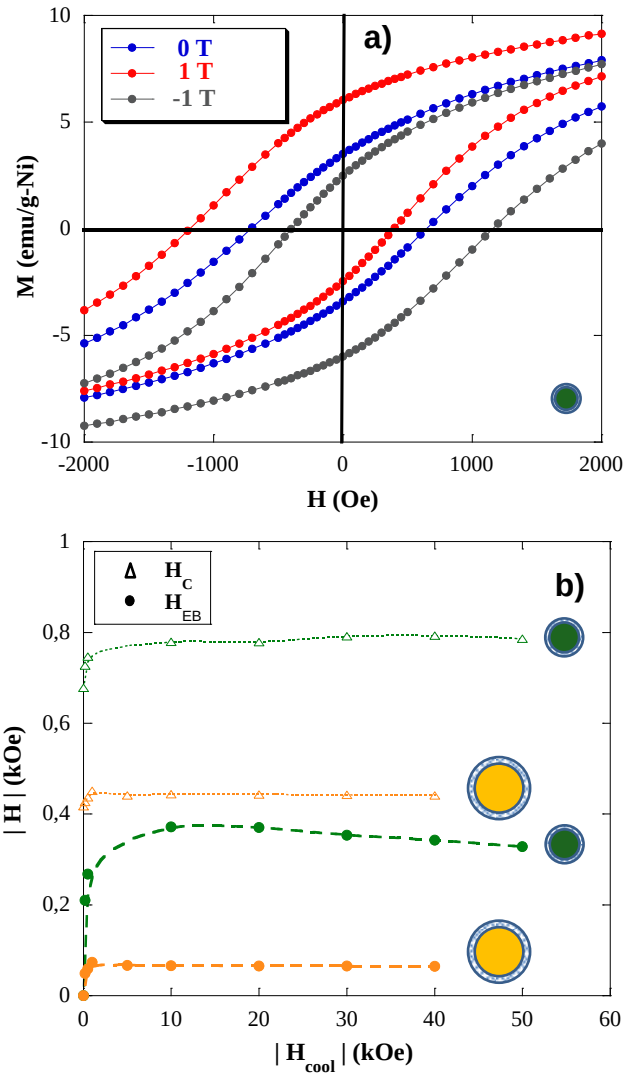

Figure 7. (a) Shifts of the hysteresis loops measured for sample A at 5K unde r cooling fields (H_{cool}) of 1T (red dots) and -1T (blue dots), compared to the loop at H_{cool} =0 (black dots). (b) Dependence of the exchange bias (H_{EB}) (solid circles) and the coercive (H_C) (empty triangles) fields with H_{cool} for samples A (green) and C (yellow).

magnetic field from a temperature above T_N ($T_N<T<T_c$) to temperatures $T<T_N$. The hysteresis loop measured then is shifted along the field axis in the opposite direction to the cooling field and this effect is the so called exchange bias (see figure 7a). In addition, an increase in the coercivity (H_C) after the field cool

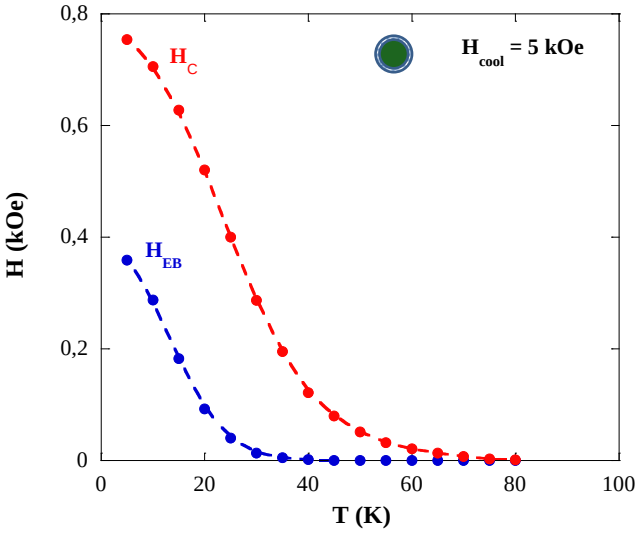

Figure 8. Temperature dependence of the exchange bias (H_{EB}) (blue dots) and the coercive (H_c) (red dots) fields, measured at H_{cool} = 5 kOe for sample A.

procedure is detected (see figure 7b). The EB can be described in the following terms: when applying a field at $T_N<T<T_c$, the spins in the shell are oriented randomly in a paramagnetic state, meanwhile the spins in the FM core are aligned along the direction of the field. When decreasing the temperature, the spins in the shell align parallel to those of the adjacent FM layer, due to the exchange anisotropy at the interface. The rest of the shell follows the AFM sequence, so that it gives a zero net magnetization. When reversing the field, the FM core gets pinned by the spins in the interface which exert an additional torque on them, so they need to overcome a field higher than the applied one. If the field is rotated back to its original direction, the FM spins will start to rotate at a smaller field because now the AFM spins exert a torque in the same direction of the field. In order to determine the equivalent temperature and field at which the exchange interaction at the FM/AFM interface is broken, both the temperature and the cooling field (H_{cool}) dependence of the exchange bias field (H_{EB}) are measured. Figure 7b shows that H_{EB} reaches a maximum at ~ 10 kOe for sample A and sample C measurements, even if the H_{EB} of the high particles is a third of that of the small ones. This can be explained by means of the number of FM spins pinned at the interface, which decreases when increasing the size of the NP. Finally, in figure 8 the decrease of the coercive field (H_C) and the EB field with temperature are plotted, for a cooling field near the maximum (5 kOe); at approximately 25 K the H_{EB} is almost extinguished.

5. CONCLUSIONS

It has been proved that it is possible to fabricate nickel nanoparticles (NPs) embedded in a carbon porous matrix by means of an easy single step reaction, by the pyrolysis of active carbon and nickel nitrate. Also, the absence of sucrose in the synthesis process gives rise to the oxidation of the NPs when exposing them to air; as a result, they exhibit a Ni core- NiO shell morphology. By using different techniques, we have showed that the effects of the oxidation process are much more relevant in small NPs, because just surface Ni atoms get oxidized and the ratio between surface and volume atoms increases when lowering the particle size. The most important consequences of the oxidation are a noticeable reduction of the saturation magnetization of the samples, compared to that of bulk Ni, and the presence of an enhanced and non-saturated magnetic response of small NPs at low temperature. Finally, the exchange coupling at the interface between the FM core and the AFM shell results in an exchange bias effect that shows a maximum of about H_{cool}^{max} ~ 0.4 kOe at 5K under a cooling field, H_{cool} ~ 10

kOe. One important finding of our work on Ni NPs concerning the exchange bias in core/shell systems is that the cooling field dependence of this effect is clearly different from that previously found in Co-based NPs embedded in a mesoporous carbon matrix[22]. One initiative that may shed light on this feature and help to understand the microscopic picture of the exchange bias in these materials is the use of magnetic x-ray circular dichroism to monitor the temperature dependence of the Ni/NiO magnetism.

In short, the reactiveness of the carbon matrix and the magnetic behavior of the embedded NPs make this material a very promising candidate for interesting applications like magnetic separation and catalysis.

ACKNOWLEDGEMENTS

I am grateful to professors Jesús A. Blanco and Pedro Gorría (Univ. Oviedo) for their essential help in this research. All samples investigated were synthesized by A. Benito Fuertes (INCAR). I thank David Martínez Blanco (SCT's Univ. Oviedo), Imanol de Pedro and Jesús Rodríguez (Univ. Cantabria) for providing assistance with magnetic measurements. I also thank Carlos Álvarez Villa and Zakariae Amghouz (SCT's Univ. Oviedo) for the TEM and HRTEM images, respectively. In addition, I thank Beatriz Vallina (SCT's Univ. Oviedo) for XRD measurements. Finally, I thank Spring-8 for allocating beam time and Jesús Chaboy (Univ. Zaragoza-ICMA) for XANES measurements.

REFERENCES

1. Karch, J.; Birringer, R.; Gleiter, H. *Nature* **1987**, *330*, 556.
2. Gleiter, H. *Prog. Mater. Sci.* **1989**, *33*, 223.
3. McMichael, R. D.; Shull R.D.; Swartzendruber, L. J.; Bennett, L. H. *J. Magn. Magn. Mater*. **1992**, 11, 29.
4. Doyle, P. S.; Bibette, J.; Bancaud, A.; Viovy, J. L. *Science* **2002**, *295*, 2237.
5. Oliveira, L. C. A.; Rios, R.; Fabris, J. D.; Garg, V.; Sapag, K.; Lago, R. M. *Carbon* **2002**, *40*, 2177.
6. Lee, I. S.; Lee, N.; Park, J.; Kim, B. H.; Yi, Y. W.; Kim, T.; Kim, T. K.; Lee, I. H.; Paik, S. R.; Hyeon, T. *J. Am. Chem. Soc.* **2006**, *128*, 10658.
7. Gorria, P.; Sevilla, M.; Blanco, J. A.; Fuertes, A. B. *Carbon* **2006**, *44*, 1954.
8. Gu, H. W.; Xu, K. M.; Xu, C. J.; Xu, B. *Chem. Commun.* **2006**, 941.
9. Bao, J.; Chen, W.; Liu, T. T.; Zhu, Y. L.; Jin, P. Y.; Wang, L. Y.; Liu, J. F.; Wei, Y. G.; Li, Y. D. *ACS Nano* **2007**, *1*, 293.
10. Park, H. Y.; Schadt, M. J.; Wang, L.; Lim, I. I. S.; Njoki, P. N.; Kim, S. H.; Jang, M. Y.; Luo, J.; Zhong, C. J. *Langmuir* **2007**, *23*, 9050.
11. Pankhurst, Q. A.; Thanh, N. K. T.; Jones, S. K.; Dobson, J. *J. Phys. D: Appl. Phys.* **2009**, *42*, 224001.
12. Sanchez-Iglesias, A.; Grzelczak, M.; Rodriguez-Gonzalez, B.; Guardia-Giros, P.; Pastoriza-Santos, I.; Perez-Juste, J.; Prato, M.; Liz-Marzan, L. M. *ACS Nano* **2009**, *3*, 3184.
13. Gupta, A. K.; Gupta, M. *Biomaterials* **2005**, *26(18)*, 3995.
14. Li, Z.; Wei, L:; Gao, MY.; Lei, H.; *Adv. Mater*. **2005**, *17(1)*, 1001.
15. Takafuji, M.; Ide, S.; Ihara, H.; Xu, ZH.; *Chem. Mater*. **2004**, *16(10)*, 1977.
16. Sousa, MH.; Tonrinho, FA.; Depeyrot, J.; da Silva, GJ.; Lara, MCFL. *J. Phys. Chem. B*, **2001**, *105(6)*, 1168.
17. Zhao, WR.; Gu, JL.; Zhang, LX.; Chen, HR.; Shi, JL. *J. Am. Chem. Soc*. **2005**, *127(25)*, 8916.
18. Scott, JHJ.; Majetich, SA.; *Phys. Rev. B*. **1995**, *52(17)*, 12564.
19. Ang, KH.; Alexandrou, I.; Mathur, ND.; Amaratunga, GAJ.; Haq, S.. *Nanotechnology*. **2004**, *15(5*), 520.
20. Hayashi, T.; Hirono, S.; Tomita, M.; Umemura, S. *Nature*. **1996**, *381(6585*), 772.
21. Fernández-García,M. P. et al., *Phys. Rev. B*. **2012**, *81*, 094418.
22. Fernández-García, M. P.et al., *Phys. Chem. Chem. Phys*. **2011**, *13*, 927.
23. Fernández-García, M. P.et al., *J. Phys. Chem. C*. **2011**, *115(13*), 5294.
24. Park, J.; Kang, E.; Son, S. U.; Park, H. M.; Lee, M. K.; Kim, J.; Kim, K. W.; Noh, H.-J.; Park, J.-H.; Bae, C. J.; Park, J.-G.; Hyeon, T. *Adv. Mater*. **2005**, *17*, 429.

25. Carenco, S.; Boissiere, C.; Nicole, L.; Sanchez, C.; Le Floch, P.; Mezailles, N. *Chem. Mater*. **2010**, *22*, 1340.
26. Bala, T.; Gunning, R. D.; Venkatesan, M.; Godsell, J. F.; Roy, S.; Ryan, K. M. *Nanotechnology* **2009**, *20*, 415603.
27. LaGrow, A. P.; Ingham, B.; Cheong, S.; Williams, G.V.M.; Dotzler, C.; Toney, M.F.; Jefferson, D.A.; Corbos, E.; Bishop, P.T.; Cookson, J.; Tilley, R.D. *J. Am. Chem. Soc*. **2012**, *134*, 855. *Supporting Information.*
28. Curiale, J.; Granada, M.; Troiani, H. E.; Sánchez, R. D.; Leyva, A. G.; Levy, P.; Samwer, K. *App. Phys. Lett.* **2009**, *95*, 043106.
29. Tamion, A.; Raufast, C.; Hillenkamp, M.; Bonet, E.; Jouanguy, J.; Canut, B.; Bernstein, E.; Boisron, O.; Wernsdorfer, W.; Dupuis, V. *Phys. Rev. B*. **2012**, *81*, 144403.
30. Ostwald, W. **1896**. *Lehrbuch der Allgemeinen Chemie*, vol. 2, part 1. Leipzig, Germany.
31. Particle Size Analyzer ("PSA") macro for ImageJ. Version r12, 2010-01-17. Ralph Sperling. Institut Català de nanotecnologia (ICN), Barcelona, Spain.
32. Rietveld, H.M.; *J. Appl. Cryst*. **1969**, *65*, 2.
33. Morales, M.P.; Veintemillas-Verdaguer, S.; Montero, M.I.; Serna, *J. Chem. Mater*. **1999**, *11*, 3058.
34. Morales, M.P.; Serna, C.J.; Bodker, F.; Morup, S.; *J. Phys. Condens. Matter*, **1997**, *9*, 5461.
35. Roy, A.; Srinivas, V. *Phys. Rev*., **2006**, *74*, 104402.
36. Rinaldi, A.; Tessonier, J.P.; Schuster, E.; Blume, R.; Girgsdies, F.; Zhang, Q.; Jacob, T.; Bee Abd Hamid, S.; Su, D.S.; Schlog, R. *Angew. Chem. Int*., **2011**, *50*, 3313.
37. Dormann, J. L.; Fiorani, D.; Tronc, E. **2007**. *Magnetic Relaxation in Fine-Particle Systems, in Advances in Chemical Physics*, *Volume 98* (eds I. Prigogine and S. A. Rice), *John Wiley & Sons, Inc., Hoboken, NJ, USA.*
38. Néel, L. **1949**. *Théorie du traînage magnétique des ferromagnétiques en grains fins avec applications aux terres cuites*. *Ann. Géophys* **5**, 99.
39. Herpin, A. **1968**. *Théorie du Magnétism*, Presses Universitaires de France.
40. Nogués, J.; Schuller, I.K. *J. Magn. Magn. Mat*., **1999**, *192*, 203.
41. Nogués, J.; Sort, J.; Langlais, V.; Skumryev, V.; Surinach, S.; Munoz, J.S.; Baro, M.D. *Phys. Rep*., **2005**, *422*, 65.